*Geophys. J. Int.* (2005) **160,** 276–288 doi: 10.1111/j.1365-246X.2004.02484.x

# The oceanic excitation hypothesis for the continuous oscillations of the Earth

T. Tanimoto

*Institute for Crustal Studies and Department of Geological Sciences, University of California, Santa Barbara,* CA 93106, *USA.*
*E-mail: toshiro@geol.ucsb.edu*

Accepted 2004 October 1. Received 2004 August 31; in original form 2004 April 6

## SUMMARY

Continuous oscillations of the Earth are observed for frequencies between 2 and 7 mHz at almost every seismically quiet site in the world. These oscillations ride on a broad noise peak which spans the frequency band from 3 to 15 mHz and reaches its maximum at 7–9 mHz. We propose an oceanic excitation hypothesis which explains both the modal oscillations and the broad noise peak, specifically the action of oceanic infragravity waves on the solid Earth. Using the estimated amplitudes of oceanic infragravity waves from observation, although they are limited in number at the moment, we show that there is sufficient energy in these waves to excite observed seismic signals; for a given time window, the contribution from a small area (which may be as small as 100 km $\times$100 km) is all that is required to explain the seismic observations. The advantage of this oceanic mechanism over the previously proposed atmospheric mechanism is in the simultaneous explanation of the above two features in seismograms, whereas the atmospheric hypothesis has only explained the modal oscillations. The oceanic mechanism naturally explains the predominant 6-month periodicity as a result of semi-hemispheric ocean-wave activities in the Northern and Southern hemispheres, showing a good match between seismic data and satellite ocean-wave data both in the amplitude and phase of seasonal variation. Our Earth seems to be filled with ubiquitous propagating Rayleigh waves, generated directly by oceanic infragravity waves, for the frequency band 3–15 mHz.

**Key words:** eigentheory, oceans, normal modes, seismic noise.



## 1 INTRODUCTION

By analysing high-quality global broad-band seismic instruments, Peterson (1993) documented basic characteristics of seismic noise and created a very useful reference model. Fig. 1 shows his model, the new low-noise model (NLNM), for frequencies between 1 mHz (millihertz) and 10 Hz. The arrow in the figure points to the frequency band of the subject of this paper. As is well known, this frequency band is sandwiched between two major seismic noise frequency bands, one for frequencies below 2–3 mHz and the other at about 50–200 mHz (peak at a period of about 7 s). The causes of these peaks are basically known; the former is caused by atmospheric effects (Warburton & Goodkind 1977; Zürn & Widmer 1995) and the latter by ocean waves (and often referred to as microseisms) (Longuet-Higgins 1950; Gutenberg 1951; Hasselmann 1963).

In this paper we focus on the cause of the small peak indicated by the arrow in Fig. 1. This peak is commonly found in vertical component seismograms at seismically quiet sites in the world. It is not found in horizontal components, probably because of the higher noise level in them. Close examination of spectra in this frequency band brings out additional features, not noted at the time of the study by Peterson (1993); an example is given in Fig. 2 , which shows an average acceleration power spectral density (acceleration PSD) from 11 globally distributed stations. The NLNM model of Peterson (1993) is shown by full circles in the top panel for comparison. The bottom panel gives an expanded view of the small box in the top panel and shows that there are many continuously excited modes within the frequency band. A close match between modal peaks and the eigenfrequencies of the preliminary reference earth model (PREM) (Dziewonski & Anderson 1981) unambiguously shows that all peaks are fundamental spheroidal modes. These modes were reported for the first time in 1998 (Nawa *et al.* 1998; Suda *et al.* 1998; Tanimoto *et al.* 1998; Kobayashi & Nishida 1998) and further analyses of the characterization of modes and the mechanism of excitation have since followed (Tanimoto & Um 1999; Nishida *et al.* 2000; Roult & Crawford 2000; Ekström 2001; Tanimoto 2001; Fukao *et al.* 2002).

This example in Fig. 2 is shown to emphasize that there are two distinct features in the seismic spectra that require explanation: (1) the continuous oscillations (individual modal peaks) and (2) the broad noise peak between 3 and 15 mHz (with the maximum at 7–9 mHz). The major purpose of this paper is to present the case that the interaction between the ocean and the solid Earth, through



 

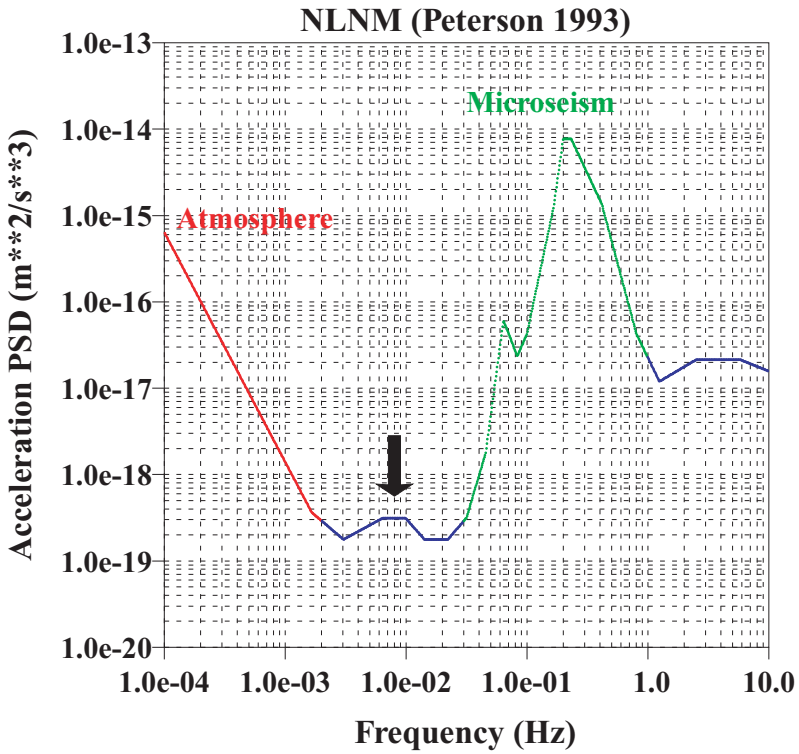


**Figure 1.** The new low-noise model (NLNM) of Peterson (1993). Seismic noise below 3 mHz (red) is dominated by atmospheric effects and noise between 30 mHz and 1 Hz (green) is dominated by ocean effects (microseisms). This paper focuses on the frequency range between 3 and 15 mHz where Peterson's model show a small noise peak, indicated by the arrow.

oceanic infragravity waves, can explain both phenomena. Previously, the cause of the continuous oscillations was argued to be the atmosphere–solid Earth interaction (Tanimoto & Um 1999; Fukao *et al.* 2002). However, the arguments in the atmospheric hypotheses have basically ignored the broad noise peak and only addressed the cause of the modal peaks; in fact, the broad noise peak was regarded as a background noise and was removed when modal amplitudes were estimated. The oceanic hypothesis in this paper can explain both features simultaneously and thus seems preferable.

It may be worth noting, however, that the atmosphere is always the ultimate source of energy, because ocean waves are excited by atmosphere–ocean interactions. The main point of our argument is that this energy must be filtered through an ocean process in order to generate the observed seismic features between 3 and 15 mHz.

After submission of the original manuscript it came to our attention that Rhie & Romanowicz (2004) had performed an observational study using two arrays of seismic networks to locate the source of the continuous oscillations. Their results indicate that the sources are related to hemispheric mid-latitude ocean-wave behaviour. This is generally consistent with our proposed mechanism, especially in explaining the modal amplitude maxima in January and July. While their study presents good observational evidence, this study presents theoretical evidence that favours the oceanic excitation hypothesis, specifically the simultaneous explanation of the amplitude behaviours of the continuous oscillations and the origin of the broad amplitude highs between 3 and 15 mHz.

In the next section we will summarize some observational features of the oceanic infragravity waves. We then derive a theoretical normal-mode formula in Section 3 and discuss some observational constraints, numerical results and their implications in Section 4.

## 2 OCEANIC INFRAGRAVITY WAVES

It was shown in the last decade that long-wavelength oceanic gravity waves, known as infragravity waves, are a ubiquitous phenomenon in the oceans (Webb *et al.* 1991; Webb 1998). These oceanic (surface) waves produce significant pressure fluctuations at the sea bottom at low frequencies because of deep penetration of energy. This is related to the fact that the eigenfunctions of these oceanic surface modes start to touch the ocean bottom at low frequencies; Fig. 3 shows three cases of oceanic surface waves at frequencies of 3.3, 10 and 20 mHz, with vertical (U) and horizontal eigenfunctions (V) computed for the earth model PREM (Dziewonski & Anderson 1981). In this model, the upper 3 km is the ocean. This figure shows clearly that the mode at 20 mHz is almost entirely confined to an oceanic layer and thus does not cause much pressure fluctuation at the ocean bottom. But ocean waves at frequencies of 10 mHz or below have significant amplitudes at the ocean bottom with associated pressure changes. These are the (linear) oceanic infragravity waves.

If infragravity waves are ubiquitous in the ocean, it means that the ocean is constantly exerting a fluctuating pressure on the solid Earth. In the model we propose below, we assume that the ocean is filled with propagating infragravity waves. The oceanic layer is regarded as an external forcing source which exerts (stochastic) pressure on the solid Earth.

For an inviscid layer with a rigid bottom boundary, pressure at the surface ($P_0$) is related to pressure at the bottom by $P_0/\cosh(kH)$ where $k$ is the wavenumber of infragravity waves and $H$ is the ocean depth (e.g. Phillips 1977). The dispersion relation of oceanic gravity waves is given by $\omega^2 = gk\tanh(kH)$ where $\omega$ is the angular frequency and $g$ is the gravitational acceleration. This formula is derived under the rigid sea-bottom boundary condition and thus,

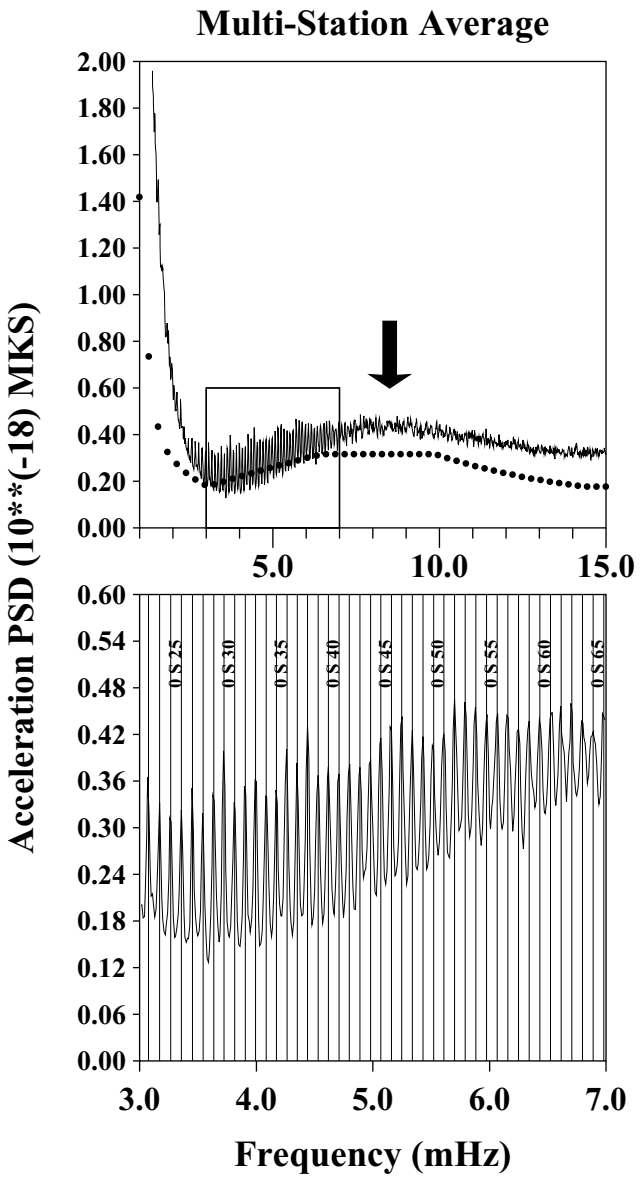


**Figure 2.** Stacked seismic spectra from 11 globally distributed stations between 1 and 15 mHz (top). The expanded view of the small box in the top panel is shown below. The modal peaks of continuous oscillations are shown to match PREM eigenfrequencies of spheroidal fundamental modes. Two features in the top figure are the focus of this paper: the broad noise peak between 3 and 15 mHz with the maximum at 7–9 mHz and the continuous oscillation peaks that emerge mainly on the lower-frequency side of this peak.

strictly speaking, is incorrect for the case of elastic boundary conditions at the sea bottom. But comparisons of the analytical rigid sea-bottom eigenfunctions with the elastic eigenfunctions (Fig. 3) show excellent agreement; differences are about 1 per cent or less and do not affect our discussions in this paper. Therefore, we will adopt the form $P_0/\cosh(kH)$ for sea-bottom pressure and use it in theory for the source of excitation.

For numerical evaluation of normal-mode formulae in the next section it is necessary to use an estimate for $P_0$, or more precisely its power spectral density $\langle P_0^2 \rangle$ (hereafter pressure PSD). In order to see its size and how it changes with geographical location we have collected published data and made our own estimates. Fig. 4 shows an example from a location near Japan (Watada *et al.* 2001); the full curve corresponds to the case $\langle P_0^2 \rangle = 3 \times 10^3$ Pa$^2$ Hz$^{-1}$ and the two dashed curves indicate $\langle P_0^2 \rangle = 10^4$ and $10^3$ Pa$^2$ Hz$^{-1}$, respectively. Interestingly, Watada *et al.* (2001) also reported atmospheric pressure changes from a barograph near this station (at the ocean surface) and its pressure spectral density which is plotted by open circles; it is clear that the atmospheric effects are lower by an order of magnitude for the frequency range in which we are interested. This is an extremely interesting observation which lends support to the oceanic excitation mechanism, but we do not go into details in this paper.

Results from two other locations are shown in Figs 5 and 6, after Webb *et al.* (1991) and Webb (1998). Fig. 5 (East Pacific Rise) shows three curves, $3 \times 10^5$ (dashed), $10^5$ (full) and $3 \times 10^4$ Pa$^2$ Hz$^{-1}$ (dashed) and Fig. 6 shows 300 (dashed), 100 (full) and 30 Pa$^2$ Hz$^{-1}$ (dashed). A summary of the estimates, including observations from other locations, is given in Table 1. The result for the last location in this table, an IRIS station H2O, is based on our analysis of data from 1999 to 2002.

While the number of data are limited, we can make some inferences based on these estimates of $\langle P_0^2 \rangle$; first of all, a large pressure PSD is of the order of $10^4$–$10^5$ Pa$^2$ Hz$^{-1}$. In the next section, we will use $10^4$ for numerical evaluation of theoretical formulae. There is also a hint that wave amplitudes are small in deep oceans and the infragravity waves are more commonly found in shallow oceans, perhaps confined to regions with depths less than 4000 m.

The latter inference is consistent with the physics of ocean-wave generation and propagation; the generation of ocean waves, obviously by atmosphere–ocean interactions, becomes efficient when the atmospheric wind velocity becomes close to the phase velocity of ocean waves. The velocity of long-period ocean waves is, roughly speaking, $\sqrt{gH}$, thus becoming small at shallow depths. $\sqrt{gH}$ is about 220 m s$^{-1}$ for 5 km ocean depth and 90 m s$^{-1}$ for 1 km ocean depth. Typical wind velocities rarely exceed a few tens of metres, but for shallow oceans this can become quite close to the velocities of ocean waves. Therefore, the generation of oceanic infragravity waves is likely to be efficient in shallow oceans.

Once generated, these waves tend to be confined to shallow oceans because of refraction due to velocity gradients; this is because waves that propagate towards deeper ocean tend to be refracted back due to velocity increase, implied in $\sqrt{gH}$. In essence, infragravity waves tend to be trapped in shallow regions (Okihiro *et al.* 1992). Therefore, the combination of generation in shallow oceans and the trapping mechanism by refraction leads naturally to the more common observation of infragravity waves in shallow oceans. These waves may reach oceans with a depth about 4000 m, however, as the result for the Atlantic Ocean in Table 1 suggests. Although these points are not proven by the data, they are certainly consistent with the results in Table 1.

## 3 NORMAL MODE FORMULA

In the proposed mechanism, the source of excitation is pressure variations at the sea bottom generated by the oceanic infragravity waves. Since the infragravity waves can be generated over multiple areas simultaneously, pressure variations are treated here as stochastic quantities both in space and time. Analysis of normal mode excitation in such a case has been published by Tanimoto & Um (1999) and Fukao *et al.* (2002) for the atmospheric excitation of normal modes. Formulae developed in these papers can be modified for the current oceanic excitation problem.

If the pressure variation on the surface is denoted by $P$, the vertical displacement in time at co-latitude $\theta$ and longitude $\phi$, $u_r(\theta, \phi, t)$, is

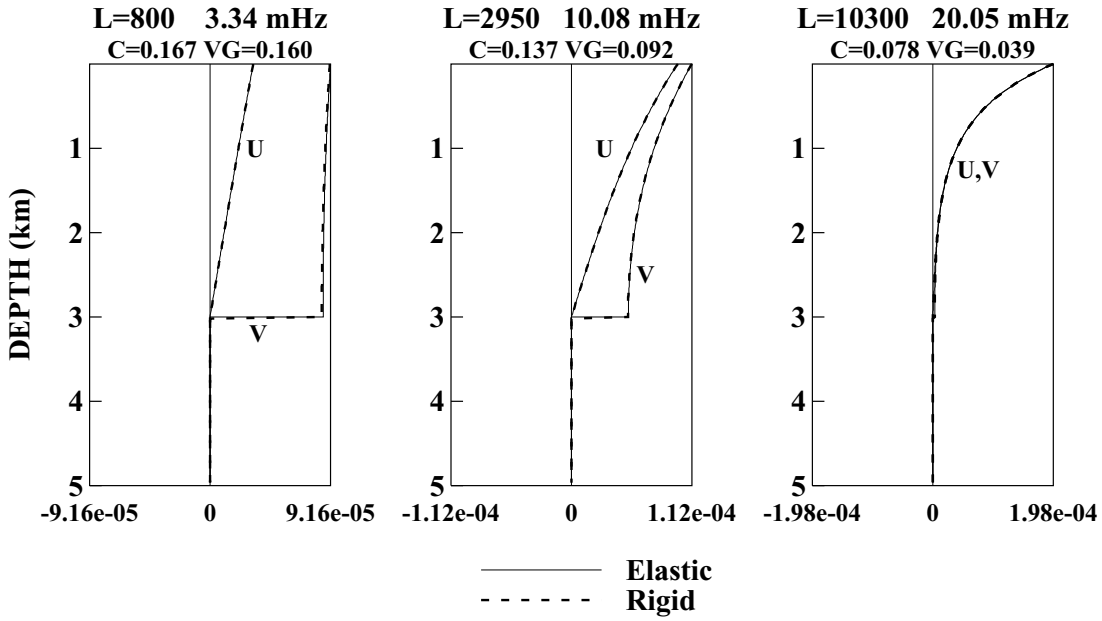


**Figure 3.** Eigenfunctions of oceanic surface waves with rigid and elastic sea-bottom boundary conditions. The top 3 km is the ocean and U and V are vertical and horizontal eigenfunctions of spheroidal modes. Dashed curves are for rigid sea-bottom solutions (analytical) and full curves are for elastic sea-bottom boundary conditions (PREM). L is the angular degree. Eigenfrequencies are given on their right-hand side in mHz. C is phase velocity (km $s^{-1}$) and VG is group velocity (km $s^{-1}$). At 20 mHz the mode is confined to the ocean. The left two modes (3.3 and 10 mHz) are the oceanic infragravity modes which generate some pressure changes at the sea bottom.

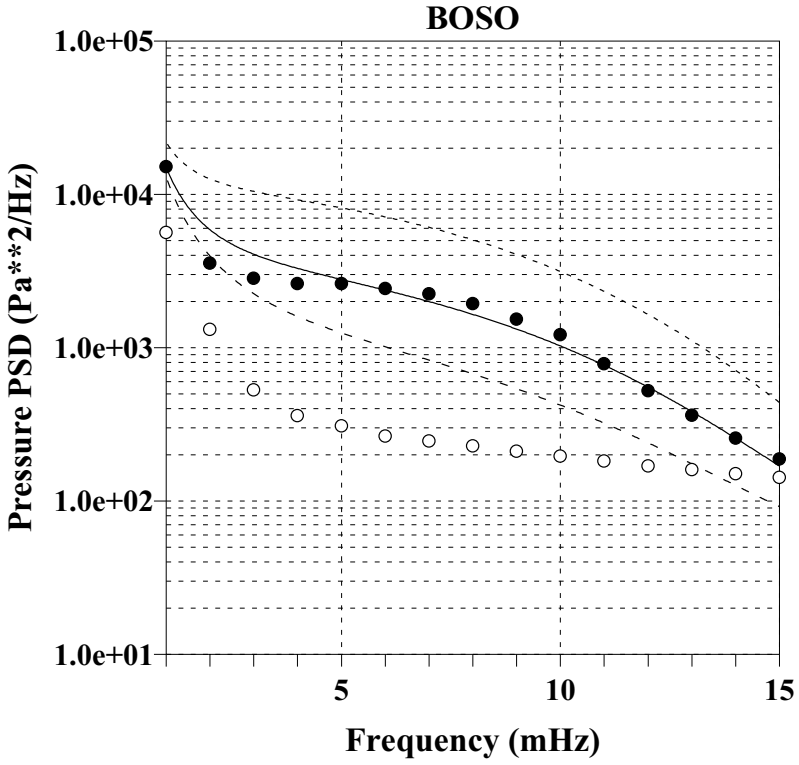


**Figure 4.** Pressure PSD at an ocean-bottom station near Japan (off the Boso Peninsula) from Watada *et al.* (2001). Full circles are ocean-bottom pressure PSD. Three curves represent $\langle P_0^2 \rangle = 10^4$, $3 \times 10^3$ and $10^3$ $Pa^2$ $Hz^{-1}$, respectively, from top to bottom. We use $3 \times 10^3$ as our best estimate (full curve). Open circles are atmospheric pressure PSD at the ocean surface near this station which is shown to be smaller by an order of magnitude.

given by

$$u_r(\theta, \phi, t) = \sum_n \sum_l \frac{U_{nl}^2(R)}{\omega_l} \sum_m a_l^m(t) Y_l^m(\theta, \phi), \qquad (1)$$

where the summations are over the overtone number $n$, the angular degree $l$ and the azimuthal number $m$, $U_{nl}(R)$ is the vertical eigenfunction evaluated at the surface (at radius $R$), $\omega_l$ is the angular eigenfrequency of normal modes, $Y_l^m$ is the spherical harmonic and

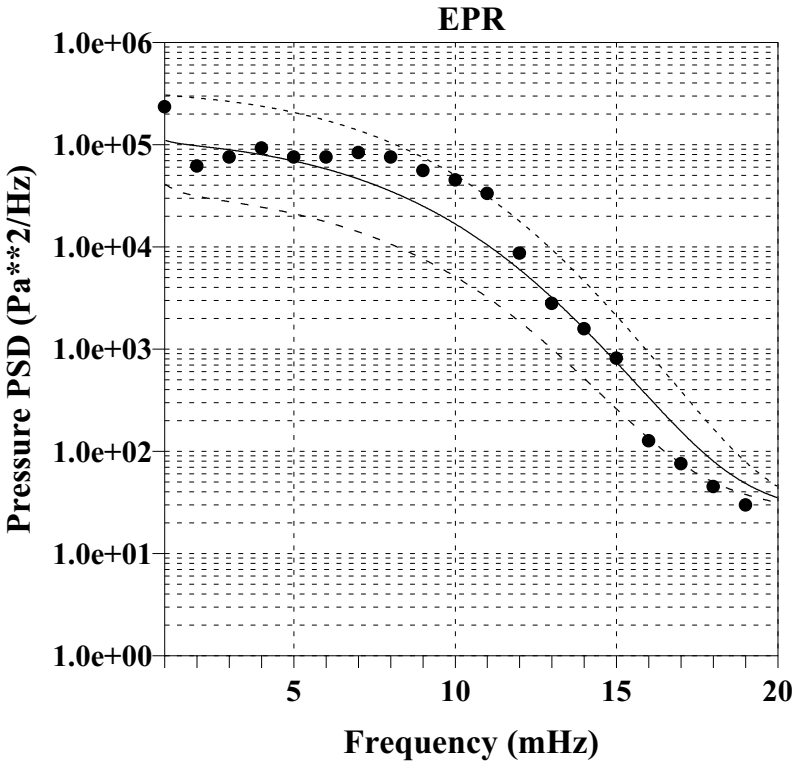


**Figure 5.** Ocean-bottom PSD data (full circles) by Webb *et al.* (1991) near the East Pacific Rise. Our best estimate is given in Table 1. Three curves are for $3 \times 10^5$ (dashed), $10^5$ (full) and $3 \times 10^4$ $Pa^2$ $Hz^{-1}$ (dashed).

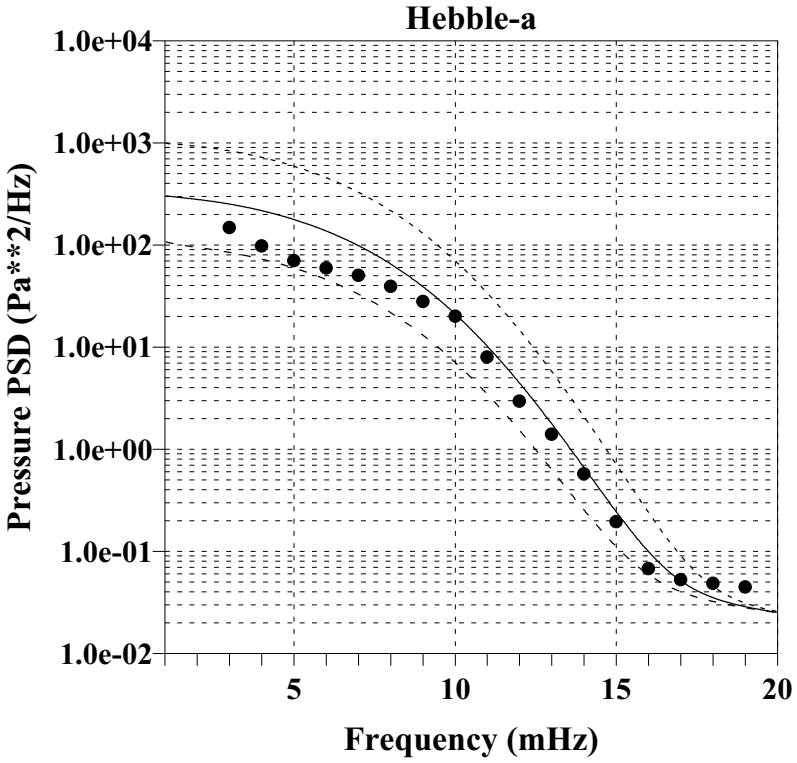


**Figure 6.** Ocean-bottom PSD data (full circles) by Webb *et al.* (1991) near Hebble (Atlantic Ocean) when ocean currents are weak. Three curves are for 300 (dashed), 100 (full) and 30 $Pa^2$ $Hz^{-1}$ (dashed).

**Table 1.** Estimate of $\langle P_0^2 \rangle$ from various regions.

| Location | Reference | Depth (m) | $\langle P_0^2 \rangle$ |
|---|---|---|---|
| Boso Peninsula | Watada *et al.* (2001) | 4000 | $3 \times 10^3$ |
| East Pacific Rise (Pacific) | Webb *et al.* (1991) (EPR), Webb (1998) (Pacific) | 3000 | $10^5$ |
| San Diego | Webb & Crawford (1999) | 800 | $10^4$ |
| Atlantic | Webb (1998) | 4000 | $10^4$ |
| Hebble-a | Webb *et al.* (1991) | 4817 | 100 |
| Hebble-b[a] | Webb *et al.* (1991) | 4817 | 30 |
| Arctic | Webb (1998) | 3000 | $\sim 0$ |
| H2O (Pacific) | IRIS data at H2O station, 1999–2002 | 5000 | $\sim 0$ |

[a]When ocean current was strong.

$a_l^m$ is defined by

$$a_l^m(t) = -\int_{-\infty}^{t} dt' \exp\left(-\frac{\omega_l(t-t')}{2Q_l}\right) \sin\omega_l(t-t') \times \int_A d\Omega' P(\theta', \phi', t') Y_l^m(\theta', \phi'). \quad (2)$$

Forming the autocorrelation function for $u_r(t)$ and introducing the pressure power cross-spectral density function $S_p(\theta', \phi', \theta'', \phi''; \omega)$ between two locations $(\theta', \phi')$ and $(\theta'', \phi'')$, we can write the power spectral density for acceleration as

$$S(\theta, \phi, \omega) = \sum_{n,n'} \sum_{l,l'} \gamma_l \gamma_{l'} \frac{U_{nl}^2(R) U_{n'l'}^2(R)}{F_l(\omega) F_{l'}(\omega)^*} \int_A d\Omega' \int_A d\Omega'' P_l(\cos\Theta') P_{l'}(\cos\Theta'') \times S_p(\theta', \phi', \theta'', \phi''; \omega) \quad (3)$$

where $\gamma_l = (2l+1)/4\pi$,

$$F_{nl}(\omega) = \left(\frac{\omega_{nl}}{\omega}\right)^2 - \left(1 + i\frac{\omega_{nl}}{2Q_{nl}\omega}\right)^2, \quad (4)$$

$Q_{nl}$ is the modal attenuation parameter, $\Theta'$ is the distance between $(\theta, \phi)$ and $(\theta', \phi')$ and $\Theta''$ is the distance between $(\theta, \phi)$ and $(\theta'', \phi'')$. Surface integral variables in (3) are $d\Omega' = R^2 \sin\theta' \, d\theta' \, d\phi'$ and $d\Omega'' = R^2 \sin\theta'' \, d\theta'' \, d\phi''$. While the above formulation incorporates contributions from overtones, the main contribution to the observed spectra arises from fundamental modes; therefore, we will drop overtones from the summations hereafter and write $\omega_l$, $F_l$ and $Q_l$ instead of $\omega_{nl}$, $F_{nl}$ and $Q_{nl}$.

We proceed to make two assumptions: (1) the correlation length in $S_p$ is the same as the wavelength $\lambda$ of the infragravity waves (typically $\sim$10 km) and (2) sea-bottom pressure PSD can be written by

$$S_p(\theta, \phi; \omega) = \frac{\langle P_0^2 \rangle}{\cosh^2[kH(\theta, \phi)]} \quad (5)$$

where $H(\theta, \phi)$ is the ocean depth at $(\theta, \phi)$. Under these assumptions, we can approximate (3) by

$$S(\theta, \phi, \omega) = \sum_{l,l'} \gamma_l \gamma_{l'} \frac{U_l^2(R) U_{l'}^2(R)}{F_l(\omega) F_{l'}(\omega)^*} \pi\lambda^2 \times \int_A d\Omega' P_l(\cos\Theta') P_{l'}(\cos\Theta') \times \frac{\langle P_0^2 \rangle}{\cosh^2(kH)} \quad (6)$$

because $\lambda$ is relatively small in comparison with the wavelengths of normal modes. Here, $\Theta'$ is the distance from a particular oceanic location to a seismic station. Integration should be extended to all relevant oceanic areas.

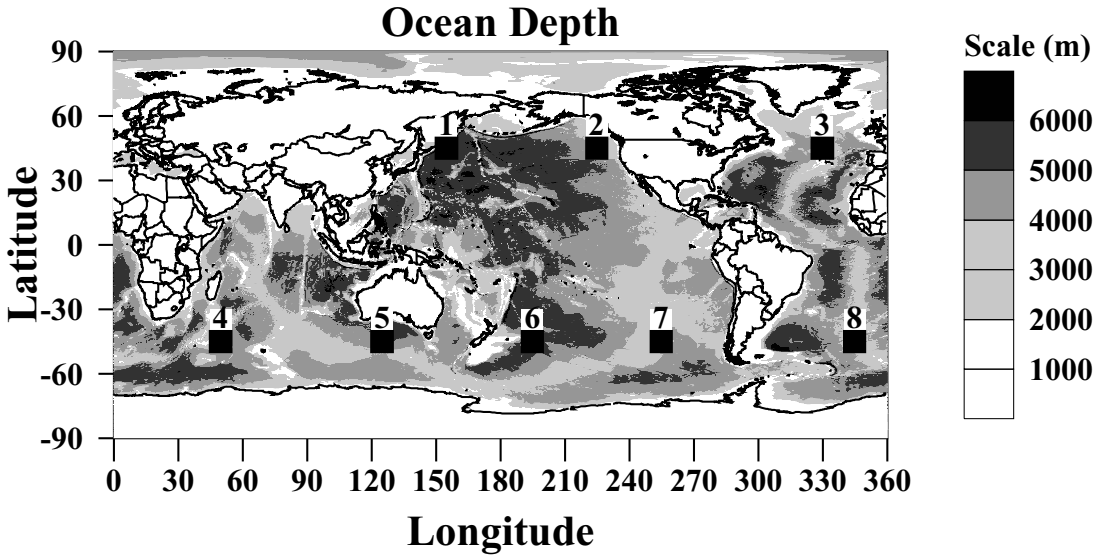


**Figure 7.** Eight source locations used for computation of the acceleration PSDs in Fig. 8. Three are in the Northern Hemisphere and five are in the Southern Hemisphere.

## 4 NUMERICAL EVALUATION

The following procedures were adopted for numerical evaluation of eq. (6); the normal-mode eigenfunctions that are needed were those of PREM. The surface pressure variations due to oceanic infragravity waves, $\langle P_0^2 \rangle$, was assumed to be $10^4$ Pa$^2$ Hz$^{-1}$. Ocean depth variations were included in the integration, for which we used averaged ocean depths over 1° by 1°.

Since we will compare theoretical results with the observed acceleration PSD in Fig. 2 , we evaluated eq. (6) at 11 locations that led to the results in Fig. 2 and took the average. For computation of theoretical PSD at each ($\theta$, $\phi$), we proceeded as follows: first, we picked an angular frequency $\omega$. For each integration over a small oceanic area the average ocean depth in the area was derived from the ocean bathymetric data and, using $\omega^2 = gk \tanh kH$, the wavenumber was determined for this $\omega$. Then, the summations over the two angular degrees, $l$ and $l'$, were performed over this small area. The maximum angular degree for these summations was $l = l' = 320$. The same procedure was repeated for all relevant regions and then the whole process was repeated for all frequencies between 3 and 15 mHz.

A straightforward integration of eq. (6) for all regions with depth less than 4000 m led to an estimate of $S(\theta,\phi,\omega)$ that is many orders of magnitude larger than the seismically observed

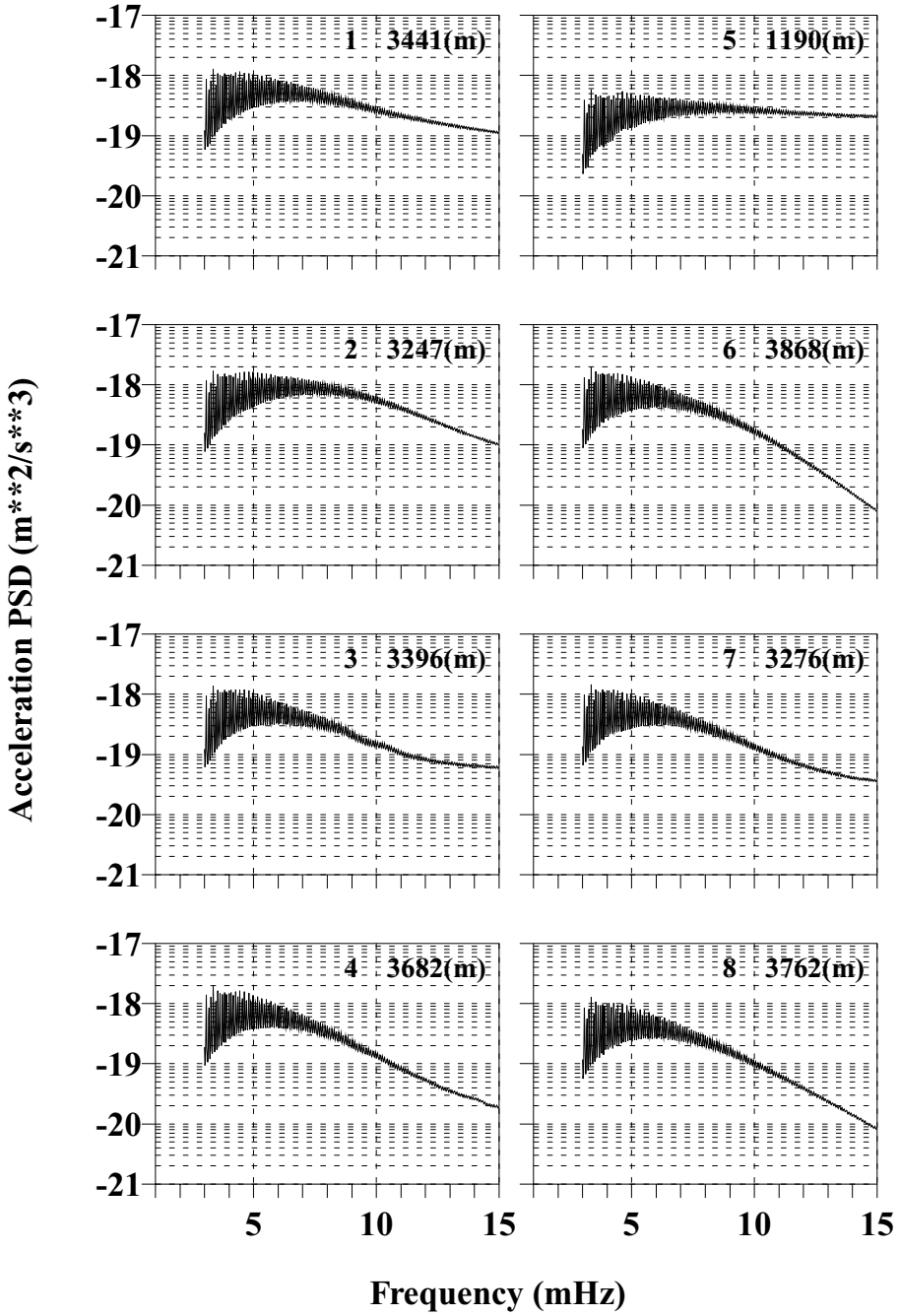


**Figure 8.** Computed theoretical seismic spectra for each source in Fig. 7. Each case has a source dimension of 100 km × 100 km. Two important features in Fig. 2 are reproduced: a broad noise peak that peaks at about 7–9 mHz and the continuous oscillation peaks that emerge on the lower-frequency side of this peak.

amplitudes in Fig. 2. The clear implication was that the contribution must be coming from a smaller region. After some trial and error, we found that an area of only 100 km × 100 km is needed to produce seismically observed amplitudes. As noted above, this estimate for the size of an area is under the assumption $\langle P_0^2 \rangle = 10^4$ Pa$^2$ Hz$^{-1}$; if we assumed $\langle P_0^2 \rangle = 10^3$ Pa$^2$ Hz$^{-1}$ instead of $10^4$, the area must be ten times larger in order to produce the same amplitudes, making it approximately 300 km × 300 km. Such a trade-off between the assumed $\langle P_0^2 \rangle$ and the 'required' area to match the observed values is obvious from eq. (6), but it is important to note that the area remains relatively small. Observed values for $\langle P_0^2 \rangle$ ($10^3$ –$10^4$ Pa$^2$ Hz$^{-1}$) place some important bounds on this point.

In order to examine the differences due to geographical location we experimented by putting the sources at eight different locations, shown in Fig. 7. Locations 1–3 are in the Northern Hemisphere and 4–8 are in the Southern Hemisphere. Each location was assumed to have an area of 100 km × 100 km with $\langle P_0^2 \rangle = 10^4$ Pa$^2$ Hz$^{-1}$. Results are shown in Fig. 8, with ID numbers (1–8) and ocean depths given in the top right-hand corners. Computed acceleration PSDs in Fig. 8 are similar to those in Fig. 2, approximately matching the maximum amplitude ($4 \times 10^{-19}$). Two main features in the observations, the existence of the broad noise peak between 3 and 15 mHz and the modal peaks on the lower-frequency side of this peak, are reproduced in most cases in Fig. 8. However, some

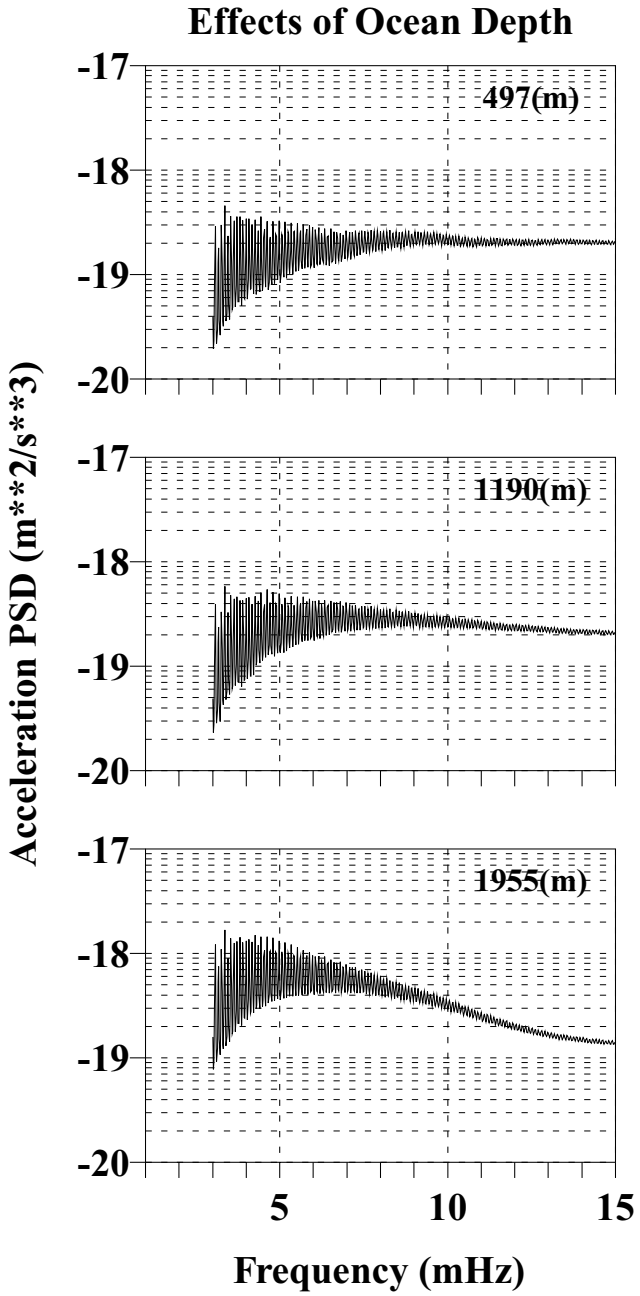


**Figure 9.** Effects of ocean depth on the acceleration PSD. The shallower the ocean, the flatter the higher-frequency asymptotes. These three locations were nearby locations, south of Australia. The middle case is the same as location 5 in Fig. 8.

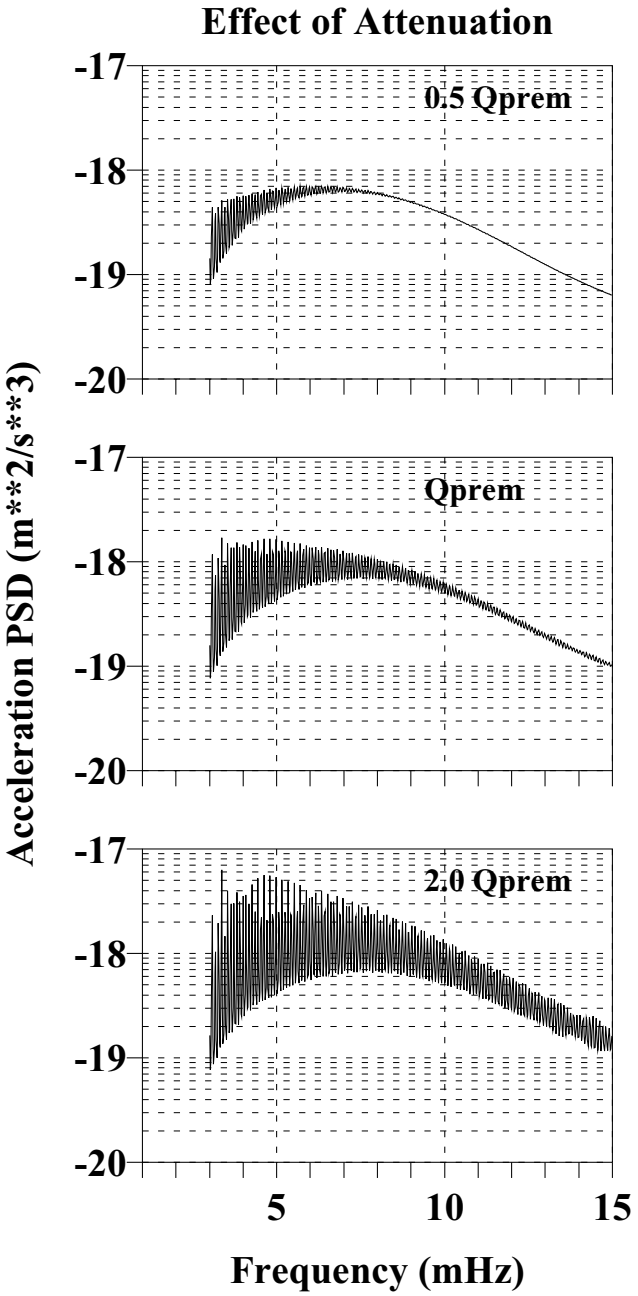


**Figure 10.** Effects of attenuation on the shape of PSD. If $Q$ is twice as large as the PREM value, modal peaks should also emerge on the higher-frequency side of the broad noise peak (bottom). The reason that we only see modes on the lower-frequency side is related to the $Q$ values in the Earth.

differences are found at higher frequencies, especially above 10 mHz; for example, the result at location 5 shows a much flatter high-frequency asymptote than the observations. This behaviour turned out to be closely related to the differences in ocean depths. In order to show this point, we calculated the acceleration PSDs at two locations, in the neighbourhood of location 5, with depths of 497 and 1955 m. These two locations are shifted to the west by 10°and 20°from location 5. Because we compute PSDs at 11 globally distributed stations and take their average, the main difference between them is ocean depth. Fig. 9 compares these three cases and shows that the high-frequency asymptotic behaviour at frequencies above 10 mHz is clearly different, making amplitudes lower with increasing ocean depth. Among them, the best match with the observed spectra in Fig. 2 is achieved for the source at a depth of 1955 m.

While this depth of about 2000 m is best for a source near location 5, it does not universally provide the best fit to the observations, however. The goodness of fit seems to change greatly with geographical location too. For example, three cases involving the Northern Hemisphere sources (1–3) are at depths of over 3000 m but seem to provide higher-frequency asymptotes that generally match the data in Fig. 2; if we choose a shallower depth region in the Northern Hemisphere, acceleration PSDs above 10 mHz become too large, compared with the observations. Thus, while a depth of about 2000 m gives a good fit for locations near 5, a depth of about 3000 m

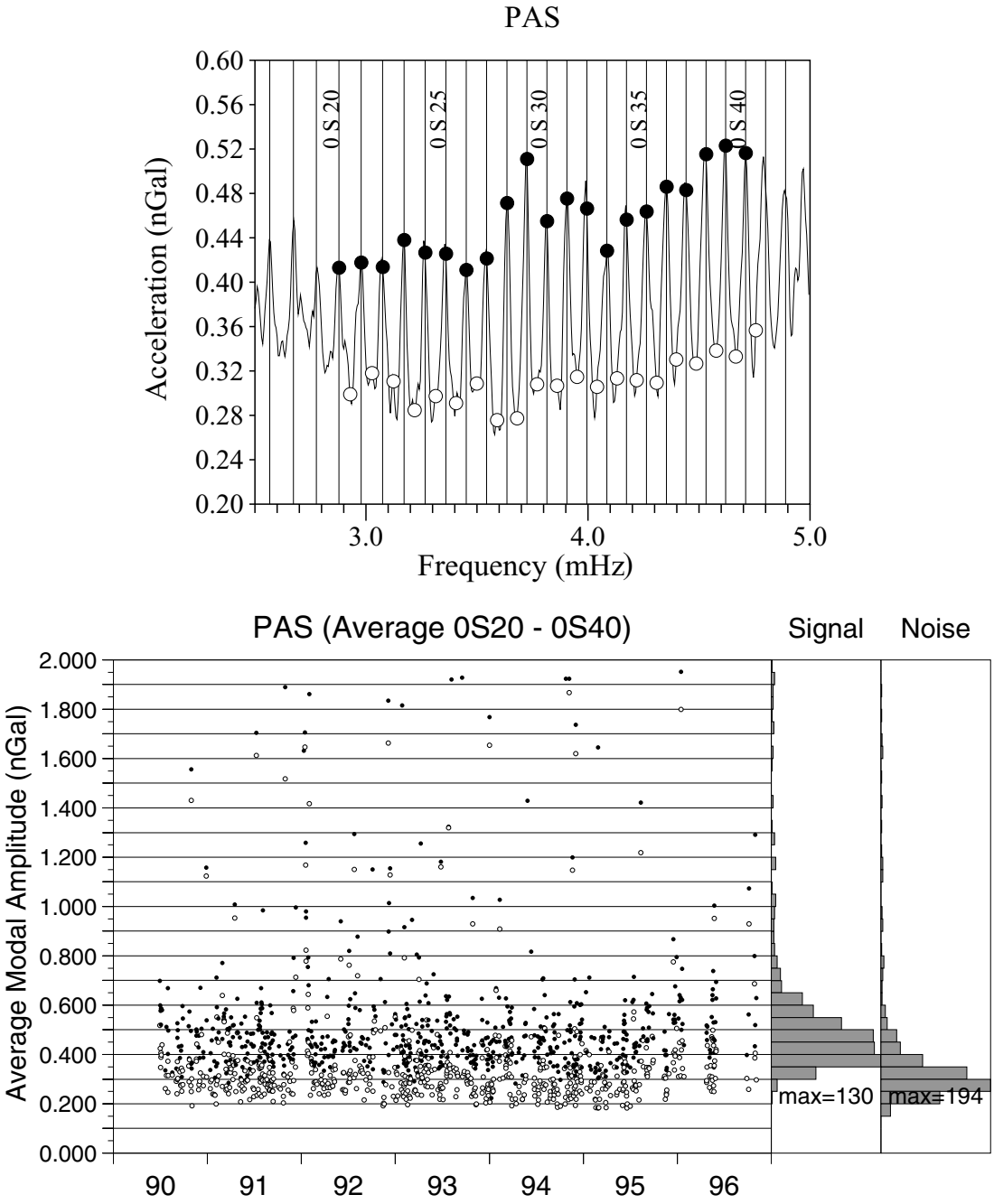


**Figure 11.** Stacking of spectral amplitudes were performed by taking the average of modal amplitudes ${}_0S_{20}-{}_0S_{40}$ every day. These numbers, computed every day, are distributed like those in the bottom panel. From this figure, we can select data that are not contaminated by earthquakes. Typically, we use the bell-shaped region in the statistics (the bottom-right panel) for further analysis.

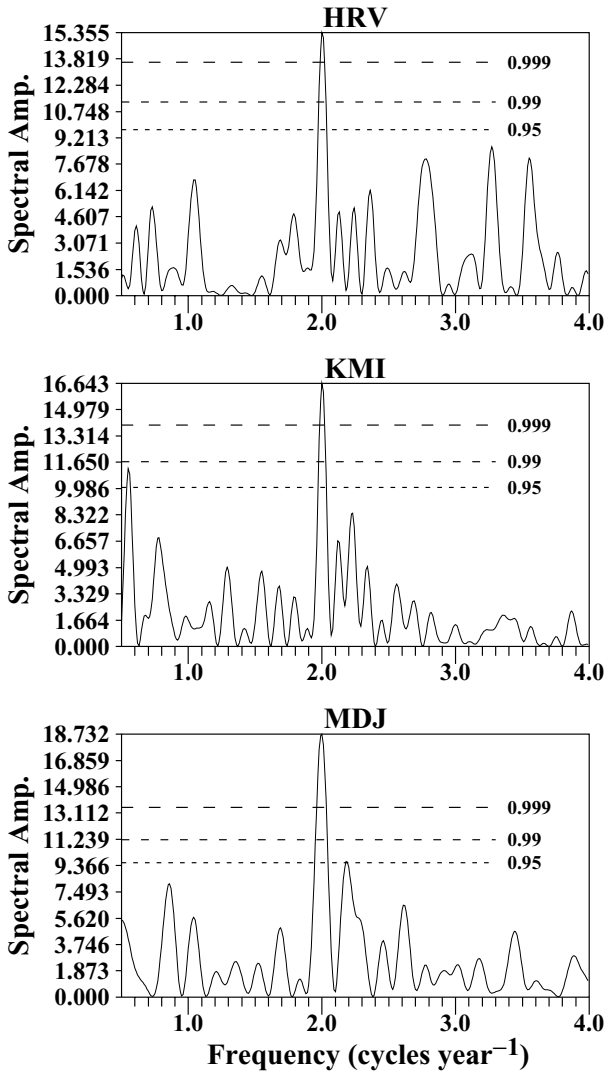


**Figure 12.** Fourier spectra of selected data in Fig. 11. All three stations display the dominant peak at 2 cycles yr$^{-1}$ or at a period of 6 months.

provides a better fit for sources in the Northern Hemisphere. Again, unfortunately, this seems to be a non-unique situation. It may suggest that the analysis of data in the form of an acceleration PSD (Fig. 2) may be insufficient for resolving the source locations and depths simultaneously.

We noted that there are some distinct differences in spectral shape if different (shear) $Q$ models are used. Fig. 10 compares acceleration PSDs for three different $Q$ models, one using half the PREM value (top), the second with the PREM value (middle) and the third with twice the PREM value (bottom). There are some differences in absolute amplitudes in Fig. 10, but the main differences between them are in spectral shape, especially in how individual modal peaks emerge out of the background broad noise; the general trend seems to be that the higher the $Q$ value the more distinct individual modal peaks become. Note that the bottom spectrum shows modal peaks distinctly all the way up to 15 mHz. Clearly, the observed acceleration PSD in Fig. 2 does not display individual modal peaks above 10 mHz, and thus the third case (twice the PREM value) does not match the data. Overall, the data seem to be consistent with a $Q$ model that is somewhat smaller than in the PREM model, although the observed spectral characteristics change to some extent depending on which stations are used for averaging.

The attenuation alone may not be the only reason for the lack of individual peaks above 10 mHz. Lateral heterogeneity can also help diminish the modal peaks because, as Rayleigh waves circle around the Earth, constructive interference of circling Rayleigh waves will be lost by complex wave propagation effects (scattering) in the heterogeneous Earth structure. Therefore, we believe that both mechanisms, the attenuation effects and the scattering effects in a heterogeneous Earth, may be contributing to the lack of individual peaks above 10 mHz.

While further clarification of the relative importance of these two mechanisms may be interesting, we believe the following recognition is far more important; that is, the reason that individual modal peaks are not seen on the higher-frequency side of the broad noise peak (7–9 mHz) is not because spheroidal modes are not excited but because of the attenuation effects and the lateral heterogeneity effects. The broad noise peak itself is actually the manifestation of spheroidal-mode energy and this spheroidal-mode energy exists

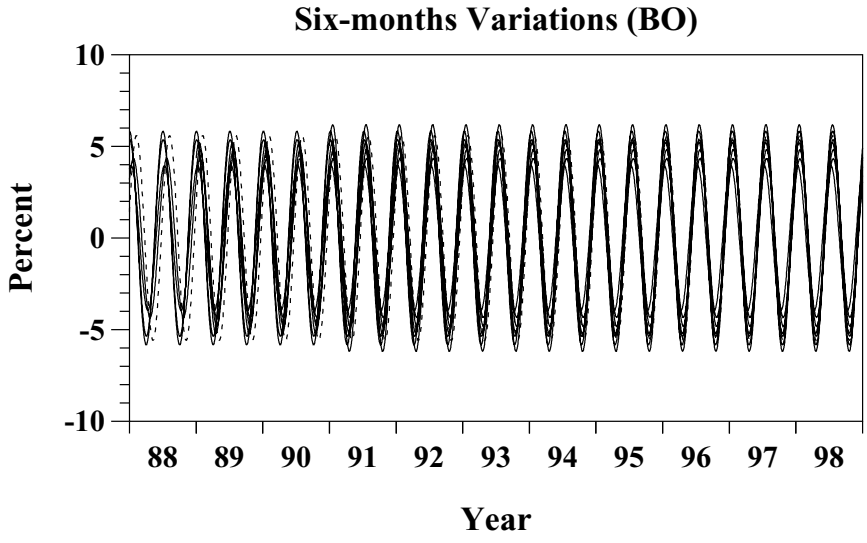


**Figure 13.** Using the phase determined from the Fourier analysis, the monochromatic time-series with 6-month periodicity are plotted. Data from nine stations are plotted including two stations in the Southern Hemisphere. All data are basically in phase, generating two peaks, one in December/January/February and the other in June/July/August. Amplitude variations are 4–6 per cent.

from 3 mHz all the way up to 15 mHz. In other words, the whole signal in this frequency band (3–15 mHz) consists of Rayleigh waves, observed everywhere on the surface of the Earth all the time. The individually observed modal oscillations are only a part of it. Our Earth is filled with these ubiquitous propagating Rayleigh waves in this frequency band.

## 5 SEASONAL VARIATIONS AND CORRELATION WITH SIGNIFICANT WAVE HEIGHT

Seasonal variations in the continuous oscillations, especially the dominant 6-month periodicity, were reported by Tanimoto (1999) and Ekström (2001). Here we show evidence of correlation between the 6-monthly variations in seismic data and those in oceanic data; oceanic data are significant wave height (SWH) from satellite data (TOPEX/POSEISDON) for the period 1997–2002.

The predominance of 6-month periodicity in seismic data was confirmed in the following way in our approach; we computed seismic spectra every day (24-hr time-series) and defined an average modal amplitude by taking the average of spectral amplitudes at eigenfrequencies of 21 spheroidal modes (${}_0S_{20}$ – ${}_0S_{40}$) using the PREM eigenfrequencies. Full circles in the top panel of Fig. 11 indicate the frequencies we chose. We determine the average amplitude for each day by this procedure. We also make the noise estimates by taking the average of the amplitudes at half-way between fundamental spheroidal modes. Open circles in the same figure indicate the results. The plot of such data between 1990 and 1996 (bottom panel, Fig. 11) shows an accumulation of data points near the bottom of this figure, making the bell-shaped distributions in the statistics. The fact that full circles are systematically higher than open circles is caused by the continuous oscillations. The data within the bell-shaped distributions are the selected data that are not likely to be contaminated by earthquake signals and are used for further analysis. Data contaminated by local or teleseismic earthquakes have higher amplitudes as some scattered points in the upper part of this figure.

We apply Fourier analysis to selected data points; because the days that are contaminated by earthquakes are eliminated from the data set, the time-series are not necessarily sampled at regular

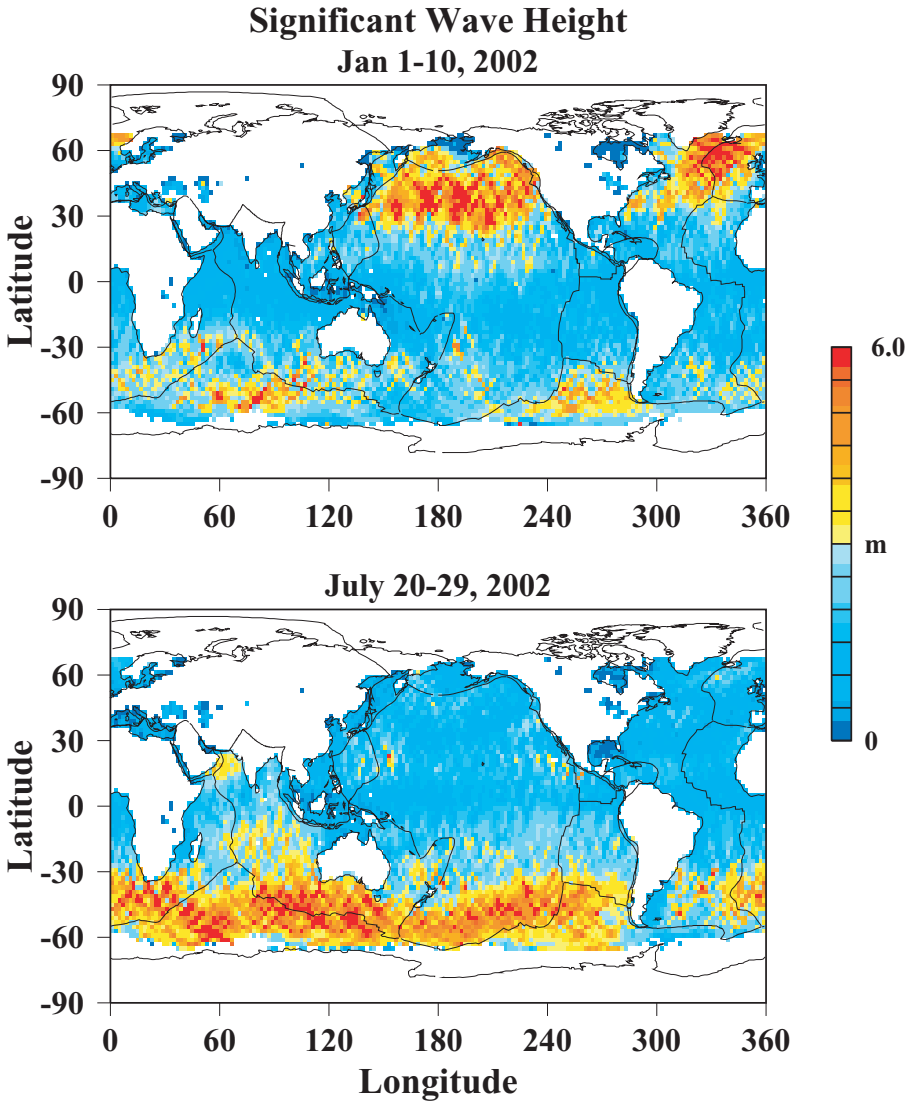


**Figure 14.** Significant wave height data from TOPEX/POSEISDON data for 2002. There is a high-amplitude band at mid-latitude in the Northern Hemisphere in January and another high-amplitude band in the Southern Hemisphere in July. The combination of these effects creates 6-month periodicity.

intervals. We thus apply a technique that can handle irregularly sampled time-series. Among many potential approaches, we adopted the Lomb–Scargle method (e.g. Press *et al.* 1986), which is a simple extension of the periodgram approach. Examples of spectra from three stations are shown in Fig. 12, which show that the dominant peaks are at 2 cycles $yr^{-1}$ or at a period of 6 months. This feature is commonly found at many other stations.

In the Lomb–Scargle method, phase can also be derived. Using the phase of 2 cycles $yr^{-1}$, we plotted the time-series from nine stations in Fig. 13. These are monochromatic time-series but all data, including the two from the Southern Hemisphere, are shown to change in phase; two peaks occur within a year, one in December/January/February and the other in June/July/August. Amplitudes of these seasonal variations vary but they are about 4–6 per cent.

Satellite data display high ocean-wave amplitudes in the Northern Hemisphere in December/January/February and in the Southern Hemisphere in June/July/August, both occurring due to high ocean-wave activities at mid-latitudes between 30°and 60°. An example from 2002 is shown in Fig. 14, which shows high amplitudes in January and in July. In order to quantify this behaviour, the integrated power (integration of the square of SWH) for both mid-latitude bands (between 30° and 60°) and for the equatorial region (between 30°S and 30°N) are shown in the top panel of Fig. 15. For each hemisphere, the dominant variation is an annual cycle. But because the peaks in each hemisphere are shifted by 6 months, the sum of all oceanic regions produces 6-monthly periodicity. The 6-month component in the Fourier analysis of integrated power from all oceanic areas is shown by the red curve in the bottom panel. In this plot, seismic results are shown by blue curves, with full curves denoting stations in the Northern Hemisphere and two dashed curves

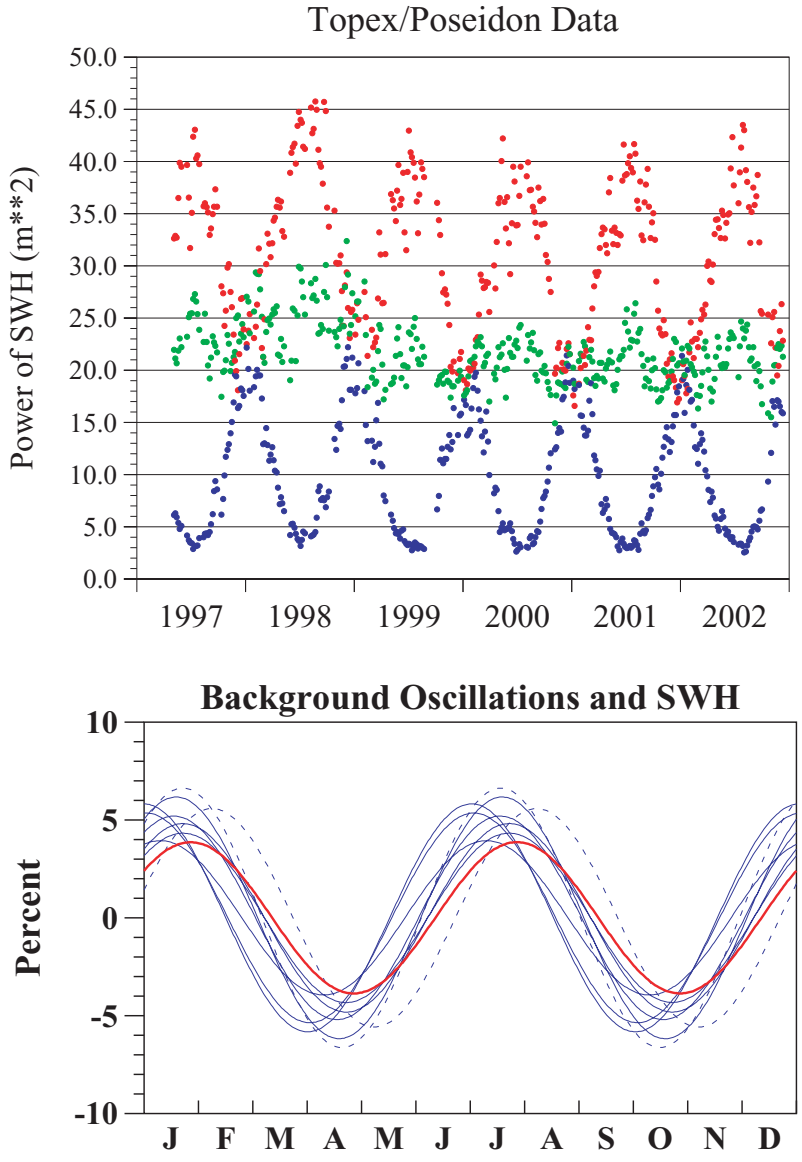


**Figure 15.** Top: Integrated ocean-wave power (square of wave height) for 1997–2002. Red is for the Southern Hemisphere mid-latitude band (between 30°S and 60°S), blue is for the Northern Hemisphere mid-latitude band (between 30°N and 60°N) and green is for the region in between (from 30°S to 30°N). Bottom: The integrated ocean-wave power for the whole region was Fourier transformed and its 6-month component is shown by a red curve. It matches with seismic data (blue curves) both in phase and amplitude. Full blue curves are from seismic stations in the Northern Hemisphere and dashed curves are those in the Southern Hemisphere.

denoting those in the Southern Hemisphere. Both amplitude and phase seem to match quite well between seismic data and ocean-wave data. There may be a suggestion of slight phase shift, but the size of this shift is within the uncertainties of this analysis.

These results clearly demonstrate that the oceanic excitation hypothesis is entirely consistent with the seismically observed 6-month periodicity. We should raise a cautionary note on this correlation, however. This is because the peak frequency of ocean-wave data (SWH) is probably caused by waves at about 100 mHz (period 10 s) whereas that of the seismic data is caused by waves at about 10 (3–15) mHz. Strictly speaking, SWH must be shown to correlate with the generation of (much lower frequency) oceanic infragravity waves. We believe it is plausible to assume this correlation but, at the moment, this is not yet proven by data. The scarcity of oceanic infragravity wave data is the critical problem.

## 6 CONCLUSION

We have proposed an oceanic excitation hypothesis for the seismic signal in the frequency band from 3–15 mHz. The two main features observed, namely the continuous oscillations and the broad noise peak, can be explained by pressure variations caused by the oceanic infragravity waves. An interesting feature is that the contribution from a small area, which may be as small as 100 km × 100 km, is all that is required to explain seismic amplitudes for a typically observed amplitude of oceanic infragravity waves. The advantage of this oceanic mechanism over the previously proposed atmospheric excitation hypotheses is in the simultaneous explanation of the modal peaks and the broad noise peak by a single mechanism. The reasons that modal peaks are seen only on the lower-frequency side of the broad noise peak are attributed to the attenuation effects and the scattering effects (complex propagation effects) in the Earth. Also this oceanic mechanism naturally explains the predominant 6-month periodicity due to semi-hemispheric ocean-wave behaviour in summer and winter, matching the amplitude and phase of seasonal variations between seismic and ocean-wave data. This feature alone, however, is not the discriminating evidence between the oceanic excitation mechanism and the atmospheric excitation mechanism because the atmosphere also has a similar hemispheric activity and thus 6-month periodicity.

Although we claim that the proposed oceanic excitation hypothesis should replace the previous atmospheric excitation hypothesis, the original source of energy must be in the atmosphere; after all, the oceanic infragravity waves are generated through atmosphere–ocean interaction. Our claim is that the original atmospheric energy must be filtered through an ocean process, i.e. through the generation of oceanic infragravity waves, in order to create seismically observable signals in the 3–15 mHz frequency band.

It is also important to note that our Earth is filled with ubiquitous propagating Rayleigh waves in this frequency band, which only becomes apparent in the absence of large earthquakes.

## ACKNOWLEDGMENTS

I thank the editor of this paper, Gabi Laske, and a reviewer, Göran Ekstrom, for their scrutiny of the manuscript and Barbara Romanowicz for sending me her preprint with J. Rhie. I also thank Doug ReVelle, Tony Dahlen, Raul Madariaga and Spahr Webb for various comments on this study. IRIS and GEOSCOPE provided superb service for seismic data retrieval for which I am really grateful. This work was mostly supported by an IGPP grant from Los Alamos National Laboratory and partially by an NSF grant (EAR-0408742) near the end.

## REFERENCES

Dziewonski, A.M. & Anderson, D.L., 1981. Preliminary reference earth model, *Phys. Earth planet. Int.,* **25,** 297–356.

Ekström, G., 2001. Time domain analysis of Earth's long-period background seismic radiation, *J. geophys. Res.,* **106,** 26 483–26 493.

Fukao, Y., Nishida, K., Suda, N., Nawa, K. & Kobayashi, N., 2002. A theory of the Earth's background free oscillations, *J. geophys. Res.,* **107**(B9), 2206.

Gutenberg, B., 1951. Observation and theory of microseisms, in *Compendium of Meteorology,* pp. 1303–1311, American Meteorological Society, Boston, MA.

Hasselmann, K.A., 1963. A statistical analysis of the generation of microseisms, *Rev. Geophys.,* **1,** 177–209.

Kobayashi, N. & Nishida, K., 1998. Continuous excitation of planetary free oscillations by atmospheric disturbances, *Nature,* **395,** 357–360.

Longuet-Higgins, M.S., 1950. A theory of the origin of microseisms, *Phil. Trans. R. Soc. Lond.,* A, **243,** 1–35.

Nawa, K., Suda, N., Fukao, Y., Sato, T., Aoyama, Y. & Shibuya, K., 1998. Incessant excitation of the Earth's free oscillations, *Earth Planets Space,* **50,** 3–8.

Nishida, K., Kobayashi, N. & Fukao, Y., 2000. Resonant oscillations between the solid Earth and the atmosphere, *Science,* **287,** 2244–2246.

Okihiro, M., Guza, R.T. & Seymore, R.J., 1992. Bound infragravity waves, *J. geophys. Res.,* **97**(C7), 11 453–11 469.

Peterson, J., 1993. *Observations and Modelling of Seismic Background Noise,* USGS Open File Report 93-322, United States Geological Survey, Albuquerque, NM.

Phillips, O.M., 1977. *The Dynamics of the Upper Ocean,* 2nd edn, Cambridge University Press, Cambridge.

Press, W.H., Flannery, B.P., Teukolsky, S.A. & Vetterling, W.T., 1986. *Numerical Recipes,* Cambridge University Press, Cambridge.

Rhie, J. & Romanowicz, B., 2004. Excitation of earth's incessant free oscillations by atmosphere–ocean–seafloor coupling, *Nature,* **431,** 552–556.

Roult, G. & Crawford, W., 2000. Analysis of 'background' oscillations and how to improve resolution by subtracting the atmospheric pressure signal, *Phys. Earth planet. Inter.,* **121,** 325–338.

Suda, N., Nawa, K. & Fukao, Y., 1998. Earth's background free oscillations, *Science,* **279,** 2089–2091.

Tanimoto, T., 1999. Excitation of normal modes by atmospheric turbulence: source of long period noise, *Geophys. J. Int.,* **136,** 395–402.

Tanimoto, T., 2001. Continuous free oscillations: atmosphere–solid Earth coupling, *Annu. Rev. Earth planet. Sci.,* **29,** 563–584.

Tanimoto, T. & Um, J., 1999. Cause of continuous oscillations of the Earth, *J. geophys. Res.,* **104,** 28 723–28 3739.

Tanimoto, T., Um, J., Nishida, K. & Kobayashi, N., 1998. Earth's continuous oscillations observed seismically quiet days, *Geophys. Res. Lett.,* **25,** 1553–1556.

Warburton, R. & Goodkind, J.M., 1977. The influence of barometric pressure variations on gravity, *Geophys. J. R. astr. Soc.,* **48,** 281–292.

Watada, S., Kobayashi, A. & Fujita, E., 2001. Seasonal variations of atmospheric and ocean-bottom pressure data in millihertz band, in, *OHP/ION Joint Symposium 'Long-Term Observations in the Oceans',* pp. 35–37. Earthquake Research Institute, University of Tokyo.

Webb, S.C., 1998. Broadband seismology and noise under the ocean, *Rev. Geophys.,* **36,** 105–142.

Webb, S. C. & Crawford, W., 1999. Long-Period Seafloor Seismology and Deformation under Ocean Waves, *Bull. Seism. Soc. Am.,* **89,** 1535–1542.

Webb, S.C., Zhang, X. & Crawford, W., 1991. Infragravity waves in the deep ocean, *J. geophys. Res.,* **96,** 2723–2736.

Zürn, W. & Widmer, R., 1995. On noise reduction in vertical seismic records below 2 mHz using local barometric pressure, *Geophys. Res. Lett.,* **22,** 3537–3540.